OXFORD

Journal of Geophysics and Engineering

Journal of Geophysics and Engineering (2023) **20**, 103–116 https://doi.org/10.1093/jge/gxac099

Effects of clay types and fractions on elastic properties of artificial clay-bearing sandstones: an experimental study

Kuizhou Li[1,2], Xuehui Han[3], Hao Zhang[4], Tao Fang[4], Xingping Luo[5] and Junguang Nie[6,*]

[1] School of Earth Science, Northeast Petroleum University, Daqing, 163000, China
[2] Research Institute of Exploration and Development of Daqing Oilfield Company, Daqing, 163000, China
[3] School of Geoscience, China University of Petroleum (East China), Qingdao, 266580, China
[4] Exploration Department of Xinjiang Oilfield Company, PetroChina, Karamay, 834000, China
[5] Research Institute of Petroleum Exploration and Development, Xinjiang Oilfield Company, PetroChina, Karamay, 834000, China
[6] School of Ocean and Earth Science, Tongji University, Shanghai, 200092, China

*Corresponding author: Junguang Nie. E-mail: njg@tongji.edu.cn

Received 19 September 2022, revised 28 November 2022
Accepted for publication 29 November 2022

Abstract

Experimentally understanding the effects of clay type and fraction on the elastic properties of clay-bearing sandstone is crucial for exploring hydrocarbon reservoirs. Therefore, we artificially synthesized a series of pure clay rocks and clay-bearing sandstones with different clay types and fractions, and conducted the ultrasonic measurements to investigate the elastic behaviors. According to experiments on pure clay rocks, illite rocks have the highest porosity, followed by montmorillonite rocks and chlorite rocks. In terms of elastic properties, illite rocks show the highest ultrasonic P- and S-wave velocities, followed by chlorite rocks and montmorillonite rocks. For clay-bearing sandstones, the measured results indicate that clay types and fractions significantly influence both the physical and elastic properties. Specifically, the porosity of chlorite-bearing sandstone is systematically lower than that of illite-bearing and montmorillonite-bearing sandstone. The chlorite-bearing sandstone has the highest P- and S-wave velocities, followed by illite-bearing and montmorillonite-bearing sandstone. Moreover, the clay fraction also affects porosity–velocity trends. The porosity first falls and then increases as the clay fraction rises, while the P- and S-wave velocities first rise and then fall and, in turn the turning point occurs at the ∼30% clay fraction. The potential mechanism of the turning point is analyzed based on the microscopic distribution of clay and sandstone. Additionally, the clay fraction and distribution also affect the electrical conductivity and permeability of the clay-bearing sandstone, implies that the clay types, clay fraction and clay distribution are non-negligible factors in reservoir evaluation.

Keywords: rock physics, clay types, clay fraction, clay-bearing sandstone

1. Introduction

Clay-bearing sandstone is the most widely distributed elastic sedimentary in the world. The presence of clay significantly affects the geophysical properties of sandstone reservoirs. Understanding the effects of clay on the elastic properties of clay-bearing sandstone is becoming increasingly essential in geophysical exploration, oil and gas field

© The Author(s) 2023. Published by Oxford University Press on behalf of the SINOPEC Geophysical Research Institute Co., Ltd. This is an Open Access article distributed under the terms of the Creative Commons Attribution License (https://creativecommons.org/licenses/by/4.0/), which permits unrestricted reuse, distribution, and reproduction in any medium, provided the original work is properly cited.

Downloaded from https://academic.oup.com/jge/article/20/1/103/6991334 by guest on 28 June 2025

development, geological disaster prevention, geological engineering, and other geoscience and engineering issues. (Nur & Byerlee 1971; Zimmerman *et al.* 1986; Crampin 1987; Main *et al.* 2000; Ehrenberg & Nadeau 2005; Healy *et al.* 2006; Yang & Hu 2020; Ba *et al.* 2015; Zuo *et al.* 2020; Guo *et al.* 2021; Qi *et al.* 2021; Liu *et al.* 2022). It is therefore necessary to quantitatively measure clay-bearing sandstone's physical properties and elastic behavior. Among them, clay types and clay fractions, as the essential components, significantly affect the elastic responses of clay-bearing sandstones.

To experimentally investigate the elastic signatures of clay-bearing sandstone and sand–clay mixtures, many peer researchers have conducted experimental measurements and theoretical modeling efforts in the past decades (Colazas 1971; Kowallis *et al.* 1984; Castagna *et al.* 1985; Han *et al.* 1986; Klimentos & McCann 1990; Marion *et al.* 1992; Hagin 2003; Li *et al.* 2019). Although both pure Ottawa sands and 50% illite-bearing Ottawa sands mixture had been experimentally measured and found that clay was a substantial factor influencing compaction state, the effects of clay types and clay fraction have not been thoroughly investigated yet (Colazas 1971). Anstey (1991) claimed that, for the loose sand packs, the clay has little influence on the bulk modulus of the rock frame but increases the density, leading to a decrease in velocities. Kowallis *et al.* (1984) experimentally investigated the relationship between the P-wave velocities and clay fraction of shaly sandstone. The results demonstrated that the P-wave velocities of shaly sandstones decrease with increasing clay fractions. They claimed that the microstructure of shale in shaly sandstone intrinsically affects its elastic velocities. Marion *et al.* (1992) synthesized artificial clay sandstone by changing the mass fraction of clay. The experimental results show that the elastic wave velocity of sandstone first increases and then decreases with the increase of clay content. Han *et al.* (1986) conducted a series of experimental measurements of artificial illite-bearing Ottawa packs (clay fraction ranging from 0 to 100%) at different confining pressure conditions. He found that both pressure histories and pressure magnitude and illite fraction can significantly influence the elastic properties of unconsolidated illite sand packs. Li *et al.* (2019) systematically investigated the relationship between dynamic elastic and anelastic properties of illite sand packs at different pressure conditions. The results demonstrated that pressure histories, clay fraction and distribution are critical factors influencing both elastic and anelastic behaviors of illite clay-bearing sand samples.

These studies examine the effects of pressure magnitude, pressure histories and clay fraction on sand–clay mixture elastic signatures. However, there is still a lack of relevant experimental measurements, which impedes an understanding and mechanism analysis of clay-bearing sandstones. Moreover, quantitative investigation of clay types' elastic properties of clay-bearing sandstones is not yet adequate (Allen & Chilingarian 1975; Nie *et al.* 2021). Therefore, in this work, we artificially synthesized pure illite, montmorillonite and chlorite rocks, and illite-, montmorillonite- and chlorite-bearing sandstone to systematically investigate both clay types and clay fraction effects on elastic properties of rock.

The structure of this work is as follows: first, we introduce our experiments, including sample preparation and ultrasonic velocity measurement. Second, we analyze the effect of clay fractions and clay types on these samples' physical properties and elastic wave velocity. Then, we discuss (i) relations between clay fraction, P-wave velocity and porosity; (ii) relations between clay fraction and clay distribution; (iii) relationships between clay types and clay distribution; (iv) the potential influence of clay fraction and clay distribution on reservoir properties and (v) possible risk for seismic interpretation. Finally, a conclusion is given.

2. Experiments

2.1. *Sample preparation*

In this work, three kinds of clay (illite, montmorillonite and chlorite with a purity of 99.9%) are purposely selected to reconstitute the pure clay rocks and sand–clay samples. The pure sands are composed of round and medium-sized quartz grains. The grain density of the quartz grain is 2.64 g cm^{-3} using a helium porosimeter.

The flow chart for building artificial clay-bearing sandstone samples is given as follows (figure 1).

(i) Weight the pure sands according to the mold size.
(ii) Mix the epoxy and curing agent with a specific ratio as for cement, then use shaking and heating to free the air bladder.
(iii) Pour the cement into pure sand, then shake and sieve to eliminate cluster cement.
(iv) Weight special ratio of clay according to the previous weight of sands, then shake and sieve to eliminate the cement–clay mixtures.
(v) Pour the clay–sand and cement mixture into the mold and then add the compression pressure of 15 MPa for 24 hours to keep the samples stable and shaped.
(vi) Put the samples in the oven at 60°C and 45% relative humidity for 24 hours to dry the cement and ensure the samples are shaped.

Here, we should point out that the general steps of building pure clay samples are similar to those of clay-bearing sandstone samples, except that in step 5 the compression pressure ranges from 5 to 25 MPa.

During these steps, the compression pressure and compression time are set to ensure the samples are stable and shaped. Furthermore, choosing a reasonable drying

Downloaded from https://academic.oup.com/jge/article/20/1/103/6991334 by guest on 28 June 2025

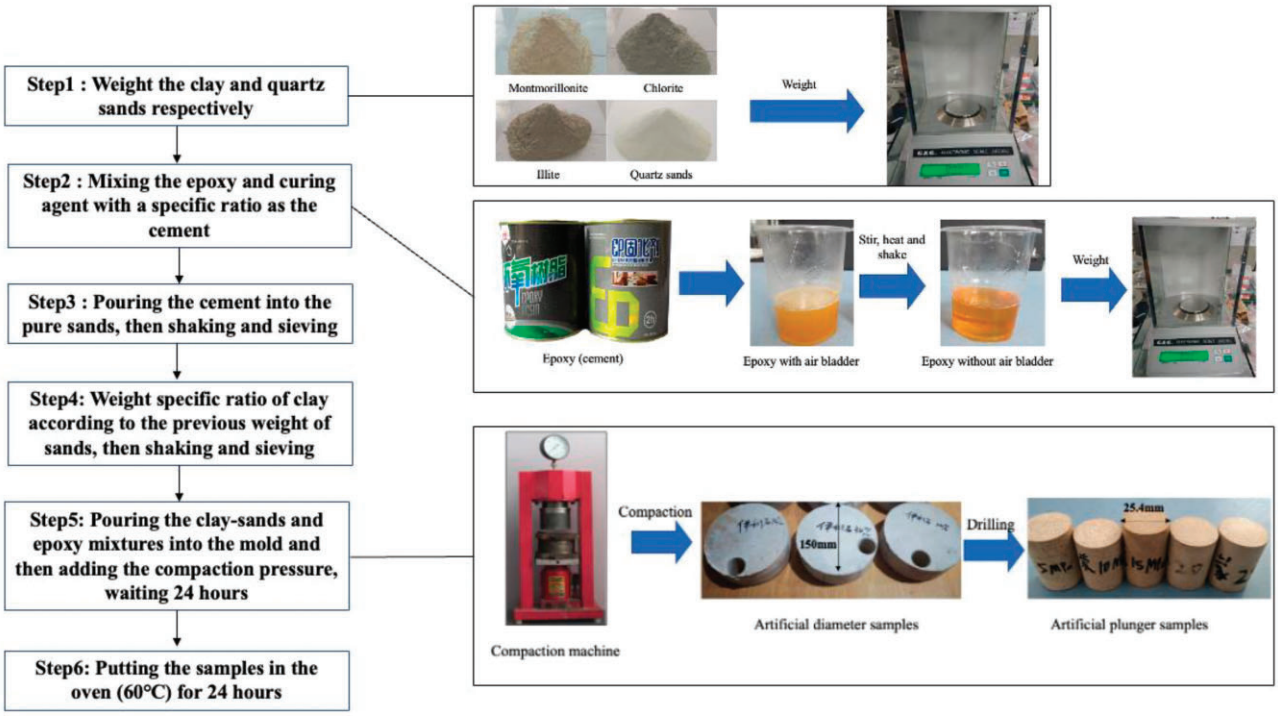

Figure 1. Flow chart to make artificial clay-bearing sandstone.

temperature is also crucial (Li *et al.* 2021): we set the drying temperature at 60°C to avoid montmorillonite dehydration, oherwise, it might generate micro cracks. We ensure adequate contact between the clay and quartz particles by multiple sievings to avoid heterogeneity as much as possible.

Furthermore, our prepared samples were full-diameter samples with a diameter of 150 mm. The samples used for research were standard plunger samples with a diameter of 25.4mm drilled from the full-diameter samples. By doing this, we try to avoid the randomness of sampling as much as possible.

Figure 2 displays the pure clay samples. Specifically, the compression pressure ranges from 5 MPa to 25 MPa. Figure 3 indicates the different clay-bearing sandstone samples at varying clay fractions at a compression pressure of 15 MPa. Porosity and ultrasonic measurements will be conducted on clay-bearing sand samples and pure clay samples in the following sections.

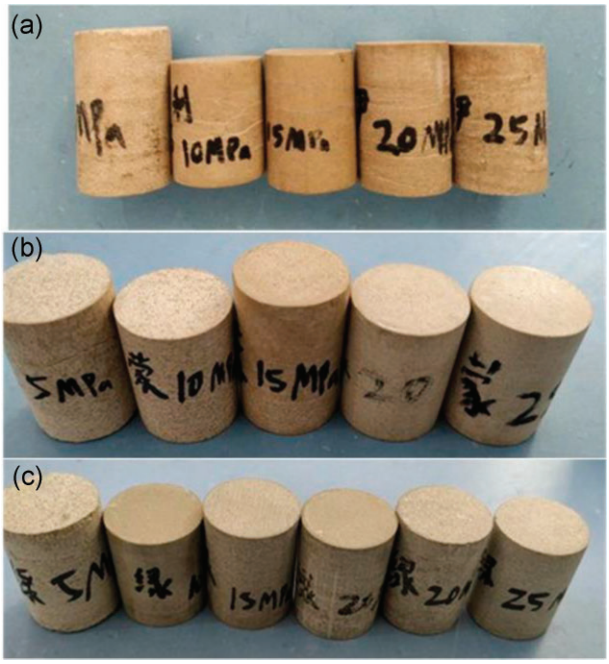

Figure 2. (a) Pure illite samples; (b) pure montmorillonite samples and (c) pure chlorite clay samples at a varying compression pressure of 5–25 MPa.

2.2. *Ultrasonic velocity measurement*

Figure 4 shows the schematic of the sample column component of the ultrasonic measurement apparatus. It mainly includes a sample assembly part, an axial linear variable differential transformer (LVDT) and confining pressure controller. Here, the axial LVDT sensor is installed to monitor the length change of the measured sample. A pair of P- and S-wave transducers are mounted at the end caps. The dominant frequencies of both P- and S-wave piezoelectric transducers are 1 and 0.8 MHz, respectively. One of them will excite ultrasonic waves with desired frequencies, which travel through the measured sample.

Downloaded from https://academic.oup.com/jge/article/20/1/103/6991334 by guest on 28 June 2025

Figure 3. Different clay-bearing sandstone samples at the compression pressure of 15 MPa.

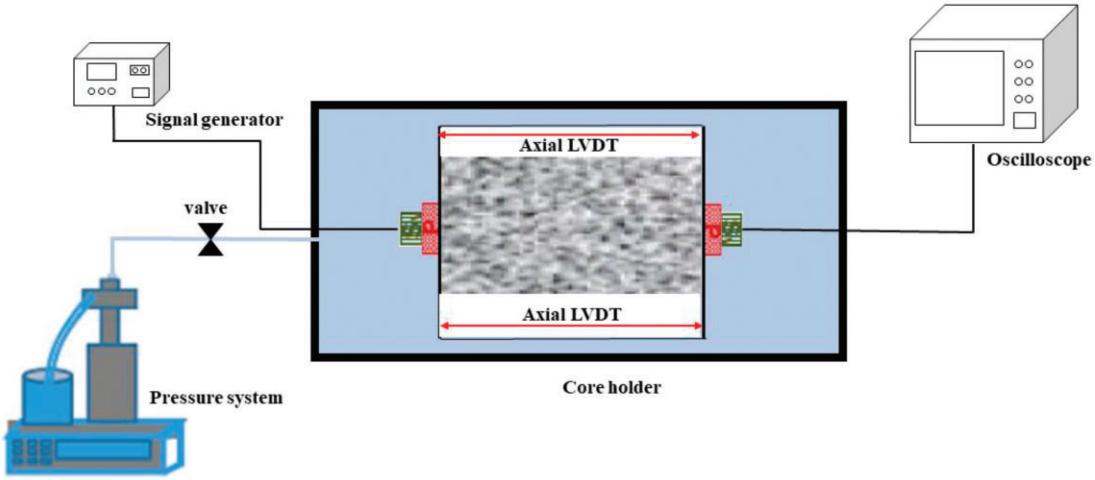

Figure 4. Schematic of the ultrasonic measurement system in this work. It mainly includes a sample clump holder and confining pressure controls.

Since the artificial sand–clay samples are easy to shorten during the measurements, the axial LVDT sensor simultaneously monitors the change of sample length, making velocity measurement more accurate. In addition, a digital pump is connected to adjust the confining pressure based on the measurement conditions.

The pulse-transmitted wave method is used to calculate P- and S-wave velocities. Namely, we can calculate P- and S-wave velocities from the recorded travel time (Δt) of the ultrasonic waves passing through the measured rock sample length (L_s). Here, we also need first to calibrate the buffer time (Δt_b) during velocity measurement. Therefore, the velocities (V) can be calculated

$$V = \frac{L_s}{\Delta t - \Delta t_b}. \tag{1}$$

With the measured bulk density (ρ_b) of rock samples, the bulk modulus (K) and shear modulus (μ) are transformed as:

$$K = \rho_b \left(V_p^2 - \frac{4}{3}V_s^2\right), \tag{2}$$

$$\mu = \rho_b V_s^2, \tag{3}$$

where V_p and V_s are ultrasonic P- and S-wave velocities of the measured rock sample, respectively.

Uncertainty is a vital factor that influences the measurement accuracy of the measured velocities. Specifically, both sample length and travel time significantly affect measurement accuracy. According to equation (1), the relative uncertainty of measured velocities is given as follows:

$$E = \sqrt{\left(\frac{U_1}{L_s}\right)^2 + \left(\frac{U_t}{\Delta t - \Delta t_b}\right)^2}, \tag{4}$$

where U_1 is the uncertainty of sample length; U_t is the uncertainty of travel time.

In this work, the uncertainty of travel time is generally 0.01 μs, the minimum travel time is 15 μs, the uncertainty of sample length is 0.005 mm and the minimum sample length is 30 mm. Therefore, the uncertainties of P- and S-wave velocities are 0.3–0.9% and 0.8–1.4%, respectively.

3. Results

3.1. *Pure clay samples*

The pure clay rocks are constructed under different compression pressure conditions to simulate the buried depth evolution process. The physical properties of pure clay pack samples are shown in Table 1.

Figure 5 shows that the porosity of pure clay pack samples decreases with increasing compression pressure first. With

Downloaded from https://academic.oup.com/jge/article/20/1/103/6991334 by guest on 28 June 2025

Table 1. Physical property parameters of pure clay pack samples

Items	Clay types	Compression pressure (MPa)	Sample volume (cm^3)	Sample weight (g)	Bulk density ($g\ cm^{-3}$)	Porosity (%)
1	Illite	5	22.258	40.096	1.801	27.402
2		10	16.360	32.742	2.001	16.041
3		15	18.318	37.600	2.053	12.042
4		20	20.050	41.335	2.062	11.193
5		25	20.117	41.492	2.063	10.605
6	Montmorillonite	5	18.767	38.174	2.034	15.922
7		10	19.739	41.906	2.123	5.814
8		15	19.579	41.593	2.124	4.683
9		20	19.427	41.326	2.127	4.224
10		25	17.766	37.910	2.134	3.981
11	Chlorite	5	19.285	41.200	2.136	13.274
12		10	16.974	38.687	2.279	2.022
13		15	18.805	43.144	2.294	1.651
14		20	18.256	41.923	2.296	1.472
15		25	17.044	39.153	2.297	1.313

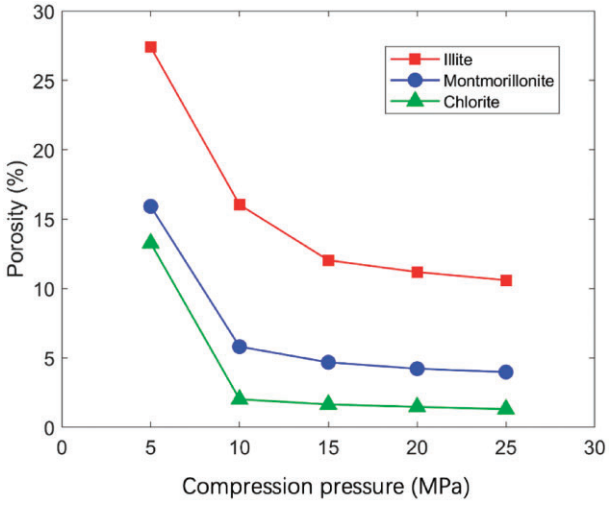

Figure 5. Porosity against compression pressure for different types of pure clay pack samples.

increasing compression pressure, the pure clay packs become stiffer, leading to a lower porosity. However, when compression pressure is beyond 15 MPa, porosities of all pure clay samples approximate a stable value, depending on clay types. Moreover, as observed, the porosities of pure illite pack samples are systematically higher than those of pure montmorillonite packs and pure chlorite packs. It implies that different clays mixing with sand may also exhibit different elastic behaviors. Meanwhile, the results also demonstrate that porosity evolution is highly dependent on both compression pressure and clay types.

We take pure clay pack samples at the compression pressures of 15 and 20 MPa as an example to measure the ultrasonic P- and S-wave velocities at varying confining pressure conditions. As shown in figure 6, the P-wave velocities of the pure clay pack samples usually increase with increasing confining pressure. However, different types of clay behave differently. As observed, the P-velocities of pure illite packs are systematically higher at the entire confining pressure range. Still, the P-wave velocities' increment slope is smoother compared with those of montmorillonite and chlorite clay packs. The P-wave velocities of montmorillonite clay pack samples are the smallest but are more sensitive to confining pressure, especially at pressures <10 MPa. Overall, the higher the compression pressure, the higher the P-wave velocities of the pure clay pack samples. S-wave velocities present a similar trend to that of P-wave velocities.

Figure 7 displays the V_p/V_s ratio of different clay packs at varying confining pressure conditions. The V_p/V_s ratio of pure montmorillonite and chlorite clay samples gradually increases with increasing confining pressure. In comparison, illite behaves oppositely and decreases with increasing confining pressure. In addition, the V_p/V_s ratio for all three types of clay samples is not sensitive to compression pressure.

3.2. *Clay-bearing sandstone samples*

Table 2 gives the physical parameters of artificial clay-bearing sand samples at the compression pressure of 15 MPa (as mentioned before, the physical properties of the samples are stable at 15 MPa) at various clay fractions from 5 to 40%. Overall, for all different clay-bearing sandstone samples, bulk density and porosity systematically vary with increasing clay fraction. Both clay types and clay fractions can be critical factors influencing the elastic properties of clay-bearing sandstone. The following analysis will detail such observations

Downloaded from https://academic.oup.com/jge/article/20/1/103/6991334 by guest on 28 June 2025

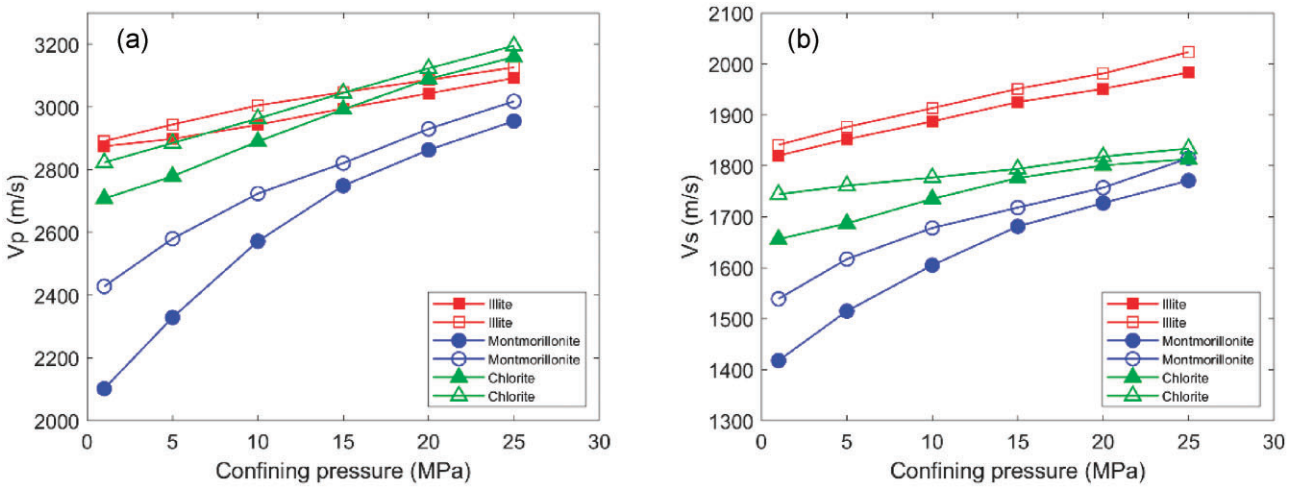

Figure 6. (a) P- and (b) S-wave velocities of pure clay pack samples against confining pressures. Note the solid symbols and shaded symbols denote compression pressures of 15 and 20 MPa, respectively.

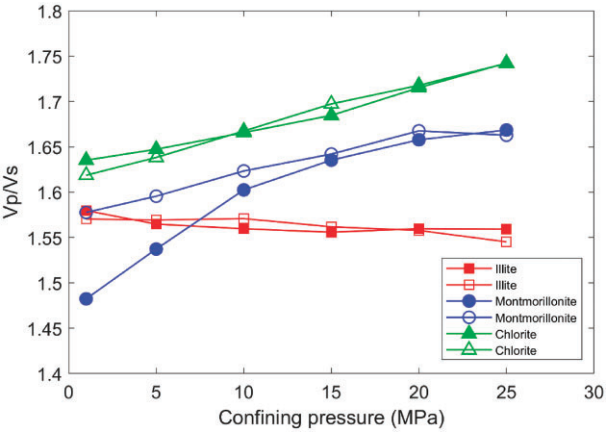

Figure 7. The V_p/V_s ratio of different pure clay pack samples at varying confining pressures.

and potential physical laws standing behind these measured data.

The correlation between the bulk density and clay fraction for these samples is shown in figure 8a. The bulk density of clay sandstone increases with an increase in the clay fraction when the clay fraction <30%; when the clay fraction is >30%, the bulk density decreases with an increase in the clay fraction. In addition, all three types of clay-bearing sample generally follow the aforementioned density–clay fraction trend. However, there still exists an obvious difference due to the clay types. Here, the bulk density of chlorite-bearing sand samples is systematically higher than those of both illite- and montmorillonite sand packs.

Figure 8b shows the relationship between the porosity and clay fraction for these clay-bearing samples. Correspondingly, the porosity of sand–clay mixture samples gradually decreases with increasing clay fraction until reaching ~30%. Then, with the continuous increase of clay fraction, the porosities of these samples seem to increase progressively with increasing clay fraction. Among them, the porosity of the chlorite samples increases more obviously. In addition, the porosity of the chlorite-sands packs is systematically lower than those of both illite- and montmorillonite-sands packs. Moreover, the porosity discrepancy among them gradually increases with increasing clay faction.

Figure 9 shows the relationship between P- and S-wave velocities of sand–clay mixture samples and the clay weight fraction for different clay types. There exists a distinct difference among different clay–sand mixture samples. Specifically, the P-wave velocities of chlorite-sands packs are systematically higher than those of both illite- and montmorillonite-sands packs. As observed, P-wave velocity increases dramatically from 0 to 10% clay content, and then the velocity increment becomes smooth when the confining pressure is between 10 and 30% clay fraction. After that, P-wave velocity begins to decrease with continuously increasing clay fraction. For illite sand packs, P-wave velocity is lower than that of chlorite sand packs. More importantly, the velocity increment is smooth when the clay fraction is <10%, while it exhibits a sharp decrement trend when the clay fraction is higher than 30% compared to that of chlorite-sands packs. For montmorillonite sand packs, the P-wave velocity is the smallest in those three different clay-bearing sand samples. Moreover, different from both illite and chlorite sand packs, the P-wave velocity of montmorillonite sand packs shows a smooth increment trend with clay fraction <20%. Then, it begins to decrease with the continuously increasing clay fraction.

Clay-bearing sands packs with different S-wave velocities have similar trends to those with P-wave velocities.

Downloaded from https://academic.oup.com/jge/article/20/1/103/6991334 by guest on 28 June 2025

Table 2. Physical parameters of artificial clay-bearing sand samples with compression pressure of 15 MPa

items	Clay types	Clay weight (%)	Sample volume (cm^3)	Sample weight (g)	Bulk density ($g\ cm^{-3}$)	Porosity (%)
1	illite	5	23.37	45.798	1.96	24.51
2		10	22.46	45.120	2.01	22.26
3		15	22.97	46.850	2.04	21.14
4		20	23.26	48.075	2.07	19.73
5		25	22.57	47.172	2.09	19.02
6		30	20.81	43.844	2.11	18.45
7		35	21.48	44.688	2.08	18.54
8		40	23.02	47.391	2.06	18.66
9	montmorillonite	5	23.45	45.495	1.94	26.19
10		10	23.15	45.607	1.97	24.34
11		15	21.58	44.027	2.04	22.36
12		20	22.08	46.586	2.11	19.59
13		25	21.23	45.211	2.13	17.84
14		30	19.30	41.683	2.16	16.93
15		35	21.10	45.145	2.14	16.95
16		40	20.73	43.745	2.11	17.22
17	chlorite	5	20.89	41.354	1.98	23.83
18		10	20.36	41.839	2.06	19.51
19		15	20.16	42.730	2.12	16.45
20		20	19.64	43.057	2.19	13.52
21		25	19.81	44.185	2.23	10.91
22		30	18.81	42.941	2.28	9.80
23		35	19.85	44.860	2.26	10.07
24		40	19.73	44.464	2.25	10.94
25	Pure sands	0	22.06	42.348	1.92	27.32

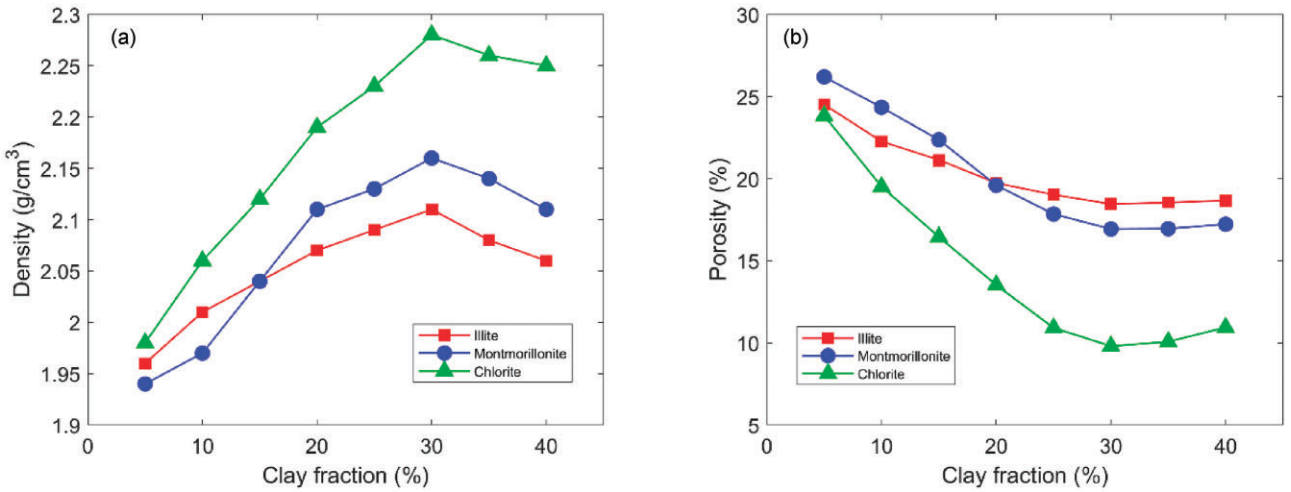

Figure 8. (a) Relationship between the bulk density and clay fraction for clay-bearing samples and (b) relationship between the porosity and clay fraction for clay-bearing samples.

Figure 10 shows the V_p/V_s ratio against clay fraction for different types of clay. The V_p/V_s ratio of the three types of clay-bearing sandstone sample gradually increases with increasing clay fractions. However, generally speaking, these samples' V_p/V_s ratios range between 1.6 and 1.7. The V_p/V_s ratio of clay-bearing sandstone is not sensitive to both clay types and clay fractions.

Figure 11a shows the relationship between P-wave velocities and porosity for these clay-bearing samples. For chlorite sand packs, P-wave velocity increases with the porosity decreasing (from 27.32 to 9.8%). Then, the velocities decrease with the porosity increase (from 9.8 to 10.94%). Overall, there are two velocity–porosity trends, which are consistent with the porosity changes shown in figure 9. There exists

Downloaded from https://academic.oup.com/jge/article/20/1/103/6991334 by guest on 28 June 2025

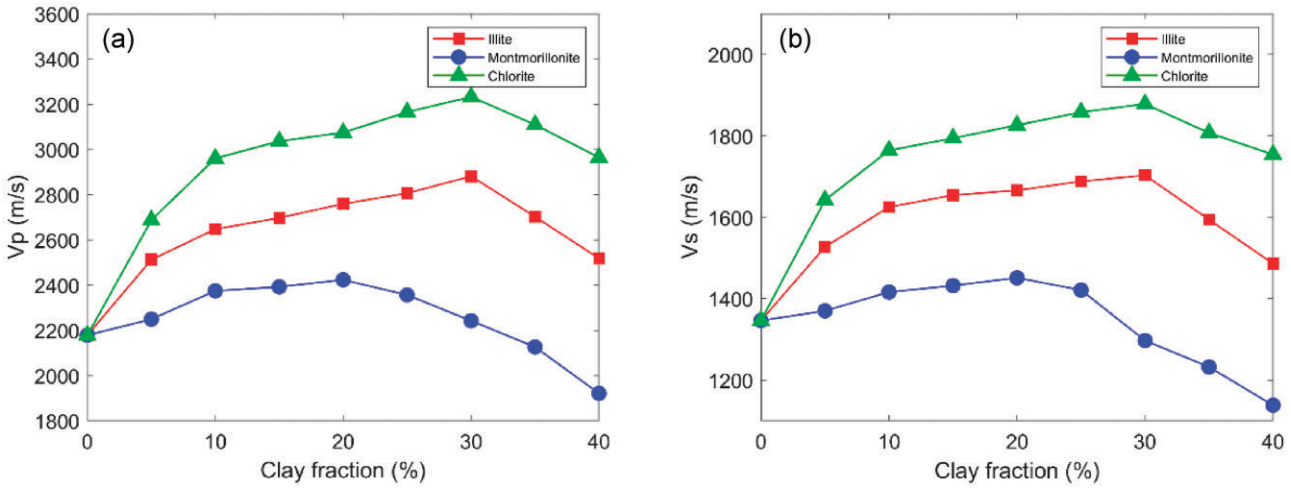

Figure 9. (a) Relationship between P-wave velocities and clay fraction for clay-bearing samples and (b) relationship between S-wave velocities and clay fraction for clay-bearing samples.

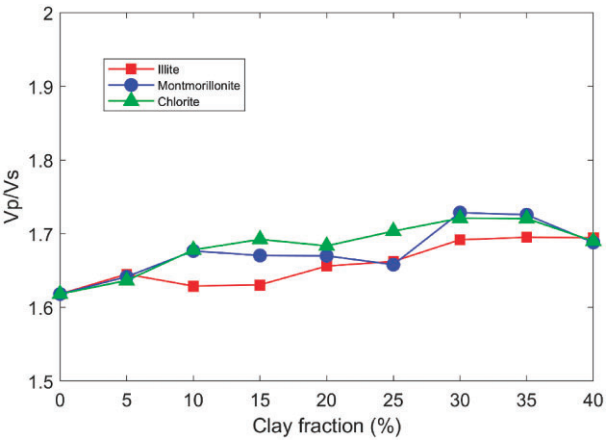

Figure 10. The V_p/V_s ratio against clay fraction for clay-bearing samples.

a turning point between these two trends with a porosity of 9.8% and a clay fraction of 30%. For illite sand packs, P-wave velocity behaves slightly different from that of chlorite sand packs. Specifically, the turning point of the P-wave velocity of illite sand packs occurs at the porosity of 18.45% and the clay fraction of 30%. For montmorillonite sandshows packs, P-wave velocity exhibits a relatively smooth change with decreasing porosity from 27.32 to 16.93%. Then it dramatically decreases with slightly increasing porosity and the turning point occurs at the porosity of 16.93% and the clay fraction of 30%.

To sum up, there exist turning points in the P-wave velocity–porosity relations of different clay-bearing sandstones. The clay fractions corresponding to the clay points are the same, but the porosity is different. Specifically, the poros-

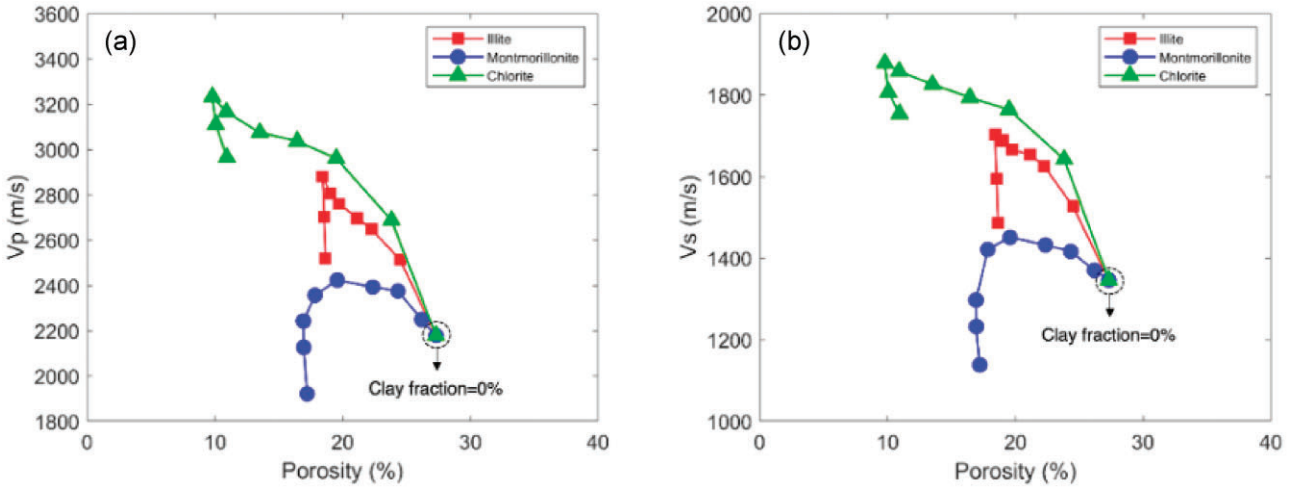

Figure 11. (a) Relationship between P-wave velocities and porosity for clay-bearing sandstone samples and (b) relationship between S-wave velocities and porosity for clay-bearing samples.

Downloaded from https://academic.oup.com/jge/article/20/1/103/6991334 by guest on 28 June 2025

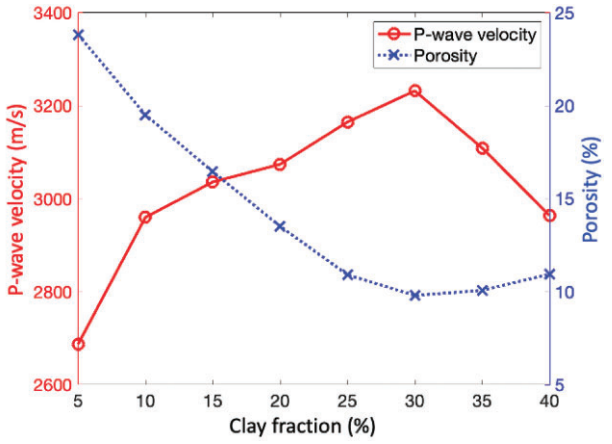

Figure 12. Cross-plot of P-wave velocity, clay content and porosity of chlorite clay-bearing sandstone. The red points and solid lines represent the P-wave velocity-clay fraction trend. The blue points and dotted line represent the porosity–clay fraction trend.

ity of the turning point of the chlorite sample is lower than that of the illite and montmorillonite samples.

Figure 11b shows that S-wave velocity presents a similar trend to P-wave velocity for three kinds of clay-bearing sand pack. The previously mentioned elastic velocity–porosity trend implies that elastic signatures of clay-bearing sands packs are highly dependent on physical properties, which are certainly related to clay types.

4. Discussion

4.1. *Relations between clay fraction, P-wave velocity and porosity*

Figure 9 shows a non-monotonic relationship between P-wave velocity and clay fraction, and the P-wave velocity increases first and then decreases with the increase of the clay fraction. Figure 8b indicates that there also exists a non-monotonic relationship between porosity and clay fraction, and the porosity decreases first and then increases with the increase of the clay fraction. These two trends are opposite. We constructed a two-coordinate cross-plot of chlorite clay-bearing sandstone to investigate the potential connection between them, as shown in figure 12. It can be seen that there is an obvious turning point at a 30% clay fraction. When the clay fraction is <30%, the P-wave velocity increases and the porosity decreases monotonously as the clay fraction increases. If the clay fraction is higher than 30%, the P-wave velocity decreases while the porosity increases with the clay fraction increasing. To further investigate the mechanism of the turning point generation, we fabricated thin sections of chlorite-bearing sandstones to observe the sand–clay distribution relations. The mechanism will be discussed in the next section.

4.2. *Relations between clay fraction and clay distribution*

Since montmorillonite-, illite- and chlorite-bearing sandstone exhibit the same porosity–velocity trend, they all have a turning point at 30% clay fraction. We only examine the microscopic distribution of chlorite-bearing sandstones. To analyze the relations between the clay fraction and the clay distribution more intuitively, we compare the thin sections (after threshold segmentation) of the chlorite clay-bearing sample under different clay fractions of 10, 20, 30 and 40%, respectively (figure 13).

It can be observed that when the clay fraction is 10% (figure 13a), the quartz particles are in direct contact and hence the rock is mainly supported by quartz particles. For clay, a small amount of clay is distributed at the contact area of quartz particles. Most of the clay is mainly attached to the surface of the independent quartz particles or distributed in the pore space, which is distributed in a dispersed state (Han *et al.* 2020; Nie *et al.* 2021).

When the clay fraction increases to 20%, the distribution of clay is not very different from that of the 10% sample; we can see that the clay occupies more pore space. However, the skeleton is still supported by quartz particles, and the properties skeleton has not changed.

When the clay fraction increases to 30%, the clay occupies more pore space. Besides, we can observe that a large amount of clay is distributed at the area where the particles are in contact, and the quartz particles are connected by clay with a non-zero contact thickness. The contact and non-contact clay exist in the rock simultaneously. Moreover, part of the skeleton is supported by connected quartz particles, while the clay-quartz sand mixture supports other parts. This phenomenon explains that the turning point in figure 12 should be caused by changes in clay distribution and the skeleton support method.

Finally, when the clay fraction increases to 40%, we can observe that the clay is distributed in clusters. The clay separates parts of the quartz particles, and the quartz particles are connected through the clay layer, forming a 'clay-packed sand' distribution form and the clay supports the frame.

In general, the lower the clay fraction, the more the clay distribution tends to be dispersed, and the support method of the skeleton is quartz-supported. The higher the clay fraction, the more clay distribution tends to be the rock matrix and the support method of the skeleton is clay-supported. This explains the non-monotonicity of the P-wave velocity-clay fraction relations and porosity–clay fraction relations shown in figure 12. Before the turning point, the dispersed clay fills the intergranular pores to decrease the porosity and increase the P-wave velocity. After the turning point, the porous clay replaces the non-porous quartz particles to support the skeleton. The inherent porosity of clay is larger than the intrinsic porosity of sands, and hence

Downloaded from https://academic.oup.com/jge/article/20/1/103/6991334 by guest on 28 June 2025

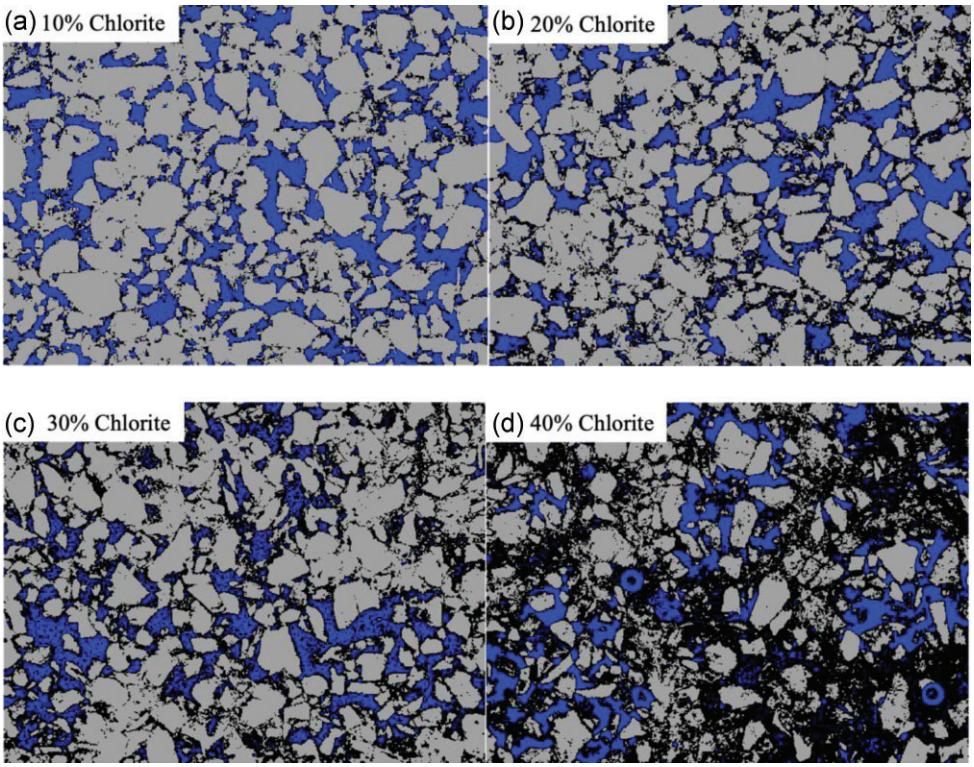

Figure 13. The thin section (after image segmentation) of chlorite clay-bearing samples with 10% (a), 20% (b), 30% (c) and 40% (d) clay fractions, where blue represents the pore space, gray represents the quartz grains and black represents the clay.

the increase in clay fraction leads to an increase in total porosity.

4.3. Relations between clay types and clay distribution

Both physical properties and elastic signatures of clay-bearing sandstone samples are closely related to the clay's location in the pore spaces and clay types. However, clay types may behave differently in terms of pore space distribution. We apply the Thomas–Stiber (TS) model to characterize the porosity–clay fraction relation of sand–clay binary mixture and corresponding rock frame evolution (Thomas & Stieber 1975, 1977; Pedersen & Nordal 1999). Figure 14 displays the TS template of the sand–clay binary mixture and the porosity of all clay-bearing sandstone samples. The porosity of clay-bearing sandstone samples gradually decreases first with increasing pore-filling clay when the clay fraction is <∼30% (line AB). Theoretically, the TS model implies that, during this stage, the rock frame is mainly composed of sand grains, whereas clay distributes dispersedly in the pore space. However, the clay will dominate the rock frame with increasing clay fraction. It is found that with clay fraction continuously adding up to 100%, the rock frame finally transformed into a clay frame with dispersed sand grains (line AC). This is consistent with the understanding obtained from the thin section of chlorite clay-bearing sandstone. In figure 8b, the porosity–

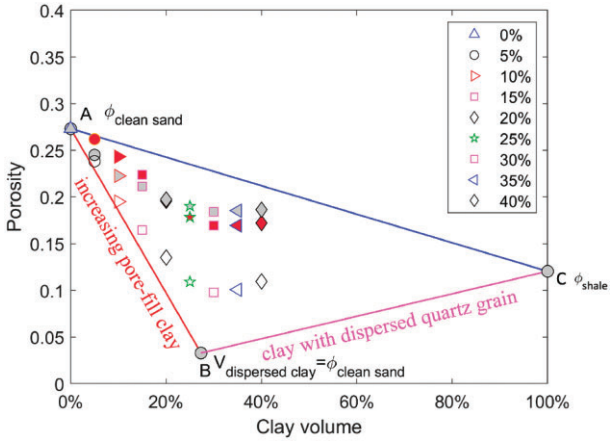

Figure 14. The TS template of sand–clay binary mixture and the measured porosity of pure and packs, 5, 10, 15, 20, 25, 30, 35 and 40% clay mixture, and 100% pure clay packs. Note that symbols with scarlet red, gray, and white represents montmorillonite-, illite- and chlorite-claying bearing sandstone with varying clay fractions, respectively.

clay fraction relations of chlorite clay-bearing sandstone are consistent with the diagnosing results of the TS model. As for montmorillonite- and illite clay-bearing sandstone samples, they behave in the same ways as chlorite. They both show a turning point at about 30% clay content, which means that the change in the support method of the skeleton is not affected by the clay types.

Downloaded from https://academic.oup.com/jge/article/20/1/103/6991334 by guest on 28 June 2025

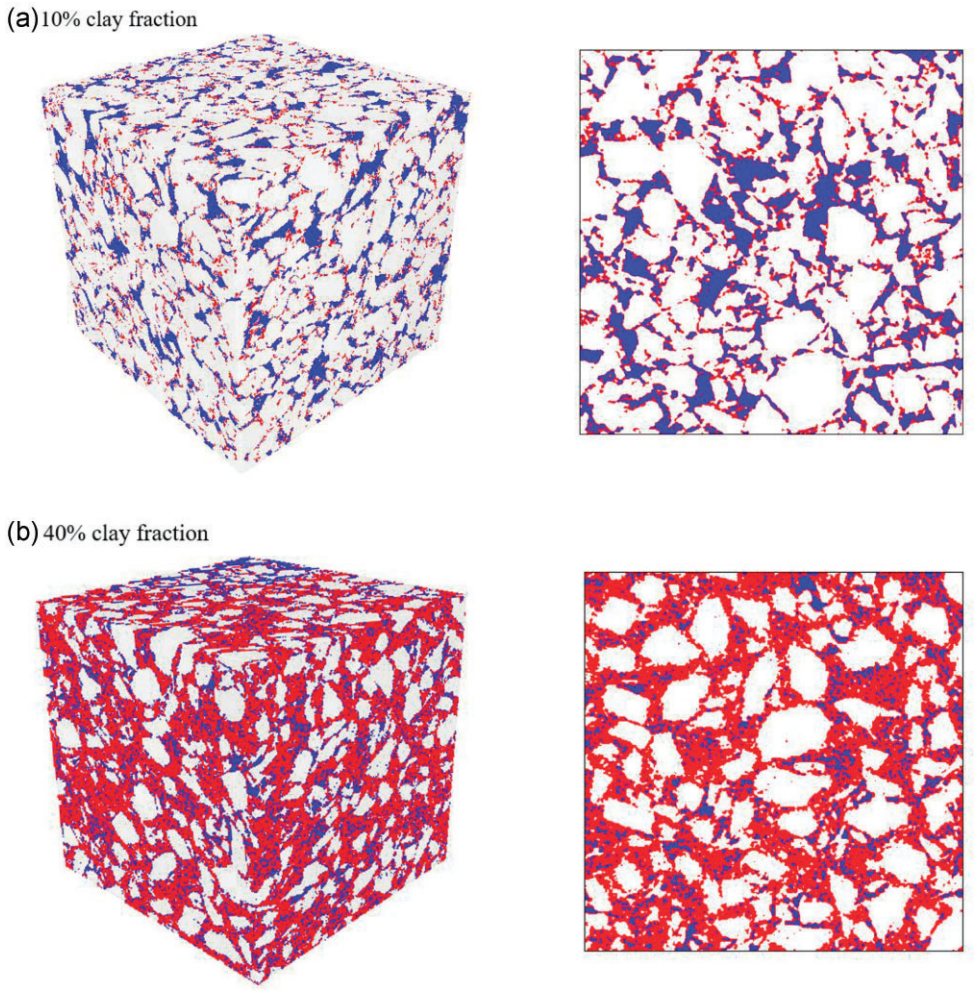

Figure 15. CT scan results of chlorite samples with 10% clay fraction (a) and 40% clay fraction (b) after threshold segmentation. The white represents the quartz particles and the blue represents the pore and the red represents the chlorite clay.

Here, we can see that the total porosity of the clay-bearing sandstone samples also increases because of the high porosity of clay itself, specifically for montmorillonite- and illite clay-bearing sandstone samples. In addition, chlorite-bearing sandstone samples closely follow the pore-filling line with lower porosity, while both montmorillonite- and illite-bearing sandstone samples tend to follow the laminated line. Overall, the TS model and measured data combination suggest that the rock frame and porosity of clay-bearing sandstone samples highly depend on clay types, clay fraction and clay distribution. However, the difference in clay types will affect the absolute value of the porosity.

4.4. The potential influence of clay fraction and clay distribution on reservoir properties

We perform computed tomography (CT) scans with chlorite-bearing sandstone samples with a clay fraction of 10 and 40%, respectively, to clarify the impact of clay content and clay distribution on reservoir properties. We use quartz, clay fraction and porosity as a reference to threshold quartz particles, chlorite and pores, and the results are displayed in figure 15. The quartz particles directly support the framework for samples with the 10% clay fraction. It is a typical grain-supported rock. For samples with a 40% clay fraction, there is almost no direct contact between the quartz particles and they are almost surrounded by clay to form typical clay-supported rock. The clay distribution of CT images is consistent with thin section images.

Then the numerical simulations of conductivity and permeability are studied. In the numerical conductivity simulation, the input potential is 1 V, output potential is 0 V and the electrical conductivity of the solution is 0.2 $S \cdot m^{-1}$. In the numerical permeability simulation, the differential pressure is set at 30 MPa and the fluid viscosity is set at 0.001 Pa·s. The numerical simulation results are shown in Table 3.

Based on numerical simulations, the difference in conductivity and formation factors is >15 times, and the difference

Downloaded from https://academic.oup.com/jge/article/20/1/103/6991334 by guest on 28 June 2025

Table 3. Numerical simulation of conductivity and permeability of chlorite samples with 10% and 40% clay fraction

Items	Clay types	Clay weight (%)	Conductivity ($S \cdot m^{-1}$)	Formation factor	Permeability (mD)
1	Chlorite	10.0	7.3×10^{-3}	27.2	70
2	Chlorite	40.0	4.7×10^{-4}	426.6	16

in permeability is more than four times. We visualized the pore seepage network based on AVIZO software, and the results are shown in figure 16. The sample with a 10% chlorite clay fraction has better pore connectivity (figure 16a and b). The pore connectivity of the sample with 40% chlorite clay fraction is worse (figure 16c and d), especially since it has many non-connected pores, which causes its lower permeability rate (Table 2).

4.5. *Potential risk for seismic interpretation*

These experimental and numerical simulation results show that different clay fractions and distributions will lead to different framework support methods (grain- and clay-supported), resulting in significant differences in reservoir properties such as conductivity, formation factor and permeability. The grain-supported rock has a higher pore space and better permeability and is the premium reservoir. The clay-supported rock, in contrast, is the non-premium reservoir. However, we notice that both the grain- and clay-supported rocks have almost the same P- and S-wave velocities

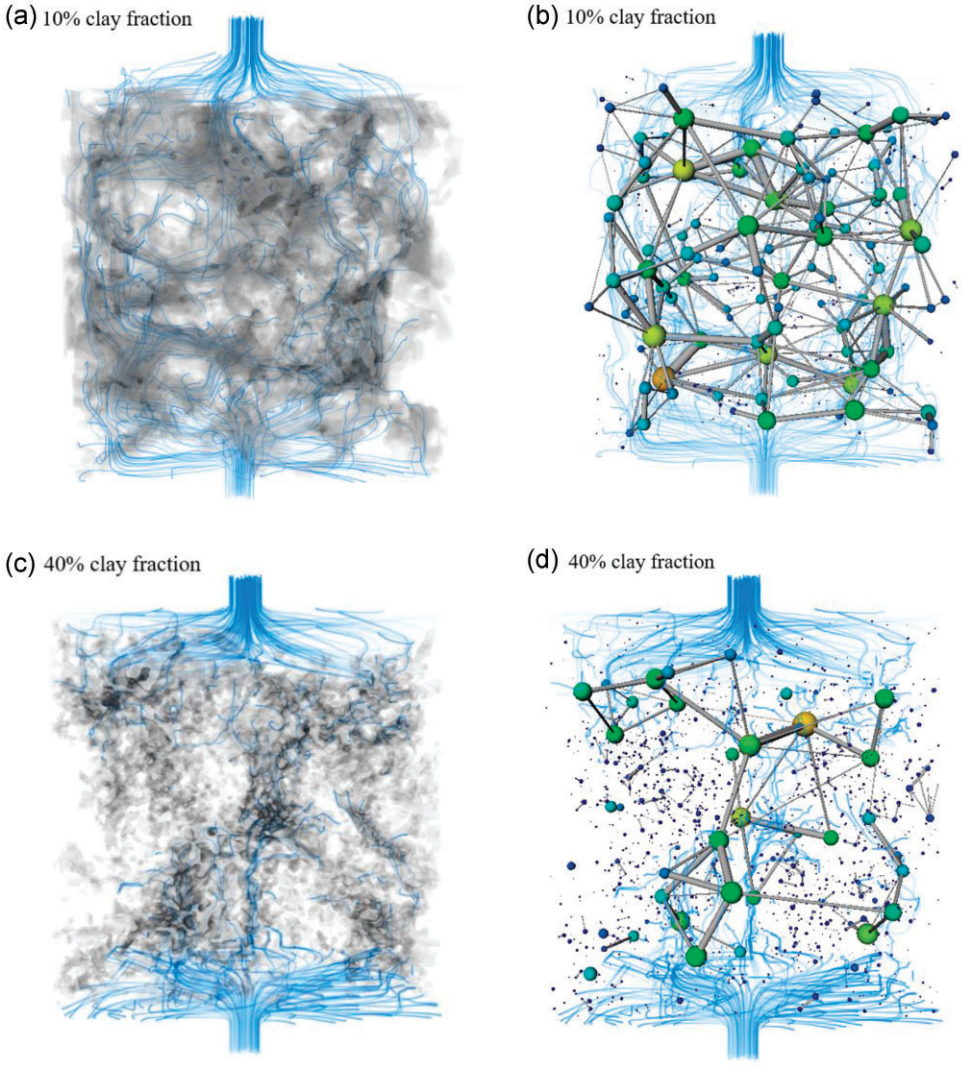

Figure 16. The visualization results of the pore seepage network and ball-and-stick model of CT scan results of chlorite samples with 10 and 40% clay fractions. The blue lines represent the seepage network, indicating the fluid's seepage path. The gray in (a) and (c) represents the pore space; in (b) and (d), the color and size of the sphere indicate the equivalent radius of the pore. The thickness of the stick represents the equivalent radius of the pore throat.

Downloaded from https://academic.oup.com/jge/article/20/1/103/6991334 by guest on 28 June 2025

(figure 9). This means that it is difficult to distinguish between the grain-supported sands and clay-supported sands from P- and S-wave velocities. The difference in the elastic properties of the two mainly depends on the density. The reliability of density inversed by seismic data is relatively insufficient. Therefore, there exist potential risks in seismic quantitative interpretation.

To reduce the risk, we recommend constructing lithological sensitivity factors such as elastic moduli or the combination of elastic parameters to amplify the difference between the grain- and clay-supported sands. More seismic attribute information is necessary to reduce the risk of reservoir evaluation in addition to elastic parameters. Moreover, we can use developed algorithms such as deep neural networks to establish the discrimination method between the two in the high-dimensional space to apply in actual reservoir evaluations.

5. Conclusions

A series of pure clay rocks samples and clay-bearing sandstone samples are synthesized experimentally to investigate their physical properties and elastic signatures with different clay fractions and clay types.

For pure clay rocks, the porosities of illite pack samples are systematically higher than those of both montmorillonite packs and chlorite packs. The P-velocities of pure illite packs are systematically higher than those of montmorillonite and chlorite clay packs. The P-wave velocities of montmorillonite clay pack samples are the smallest but more sensitive to confining pressure. Besides, the higher the compression pressure, the higher the P-wave velocities of the clay pack samples. S-wave velocities present a similar regularity to that of P-wave velocities.

For clay-bearing sandstone, the clay types and fractions influence clay-bearing sandstone's porosity and velocity trends. Specifically, the porosity of chlorite-bearing sandstone is systematically lower than that of illite- and montmorillonite-bearing sandstone. The chlorite-bearing sandstone has the highest P- and S-wave velocity, followed by illite-bearing sandstone, and montmorillonite-bearing sandstone has the lowest velocity. In addition, the trends of velocity–porosity-clay fraction of three types of clay-bearing sandstone are similar. With increasing clay fraction, the porosity first decreases and then increases while the P- and S- wave velocity increases first and then decreases; the turning point occurs at the 30% clay fraction. The mechanism of the turning point of porosity and velocity is investigated by analyzing the micro-distribution of clay and sand particle. The clay distribution causes the turning point, so the different clay distributions and fractions will lead to different framework support and a low clay fraction leads to sand support while a high clay fraction leads to clay support. Different distributions of clay have non-negligible effects on reservoir properties such as conductivity and permeability.

The study of clay type, fraction and distribution in clay-bearing sandstones can be applied to reservoir characteristics and hydrocarbon exploration of shallow surface sandstone reservoirs and unconsolidated seafloor sandstone.

Conflict of interest statement. None declared.

References

Allen, D.R. & Chilingarian, G. V., 1975. Mechanics of sand compaction, *Developments in Sedimentology*, **18**, 43–77.

Anstey, N.A., 1991. Velocity in thin section, *First Break*, **9**, 449–457.

Ba, J., Du, Q., Carcione, J.M., Zhang, H. & Müller, T.M., 2015. *Seismic Exploration of Hydrocarbons in Heterogeneous Reservoirs*. Amsterdam, Netherlands: Elsevier.

Castagna, J.P., Batzle, M.L. & Eastwood, R. L., 1985. Relationships between compressional-wave and shear-wave velocities in clastic silicate rocks, *Geophysics*, **50**, 571–581.

Colazas, X.C., 1971, *Compaction of sediments and effects of water injection, Wilmington and Long Beach offshore oil fields, PhD thesis*, University of Southern California, CA.

Crampin, S., 1987. Geological and industrial implications of extensive-dilatancy anisotropy, *Nature*, **328**, 491–496.

Ehrenberg, S.N. & Nadeau, P.H., 2005. Sandstone vs. carbonate petroleum reservoirs: a global perspective on porosity-depth and porosity-permeability relationships, *AAPG Bulletin*, **89**, 435–445.

Guo, Q., Ba, J., Cong, L. & Pang, M., 2021. Seismic rock physics inversion with varying pore aspect ratio in tight sandstone reservoirs, *Journal of Petroleum Science and Engineering*, **207**, 109131.

Hagin, P., 2003. *Application of viscoelastic, viscoplastic, and rate-and-state friction constitutive laws to the deformation of unconsolidated sands, PhD thesis*, Stanford University, CA.

Han, D.H., Nur, A. & Morgan, D., 1986. The effects of porosity and clay content on wave velocities in sandstones, *Geophysics*, **51**, 2093–2107.

Han, X., Nie, J., Guo, J., Mao, X., Luo, X., Wang, Z., Zhang, H., Liu, H., Wang, H., Jiang, J., Li, H. & Li, J., 2020. Quantitative estimation of contact cemented clay in clay-bearing sandstone and its effect on elastic properties of sandstones, *Chinese Journal of Geophysics (in Chinese)*, **63**, 1654–1662.

Healy, D., Jones, R. & Holdsworth, R., 2006. Three-dimensional brittle shear fracturing by tensile crack interaction, *Nature*, **439**, 64–67.

Klimentos, T. & Mccann, C., 1990. Relationships among compressional wave attenuation, porosity, clay content, and permeability in sandstones, *Geophysics*, **55**, 998–1014.

Klimentos, T., 1991. The effects of porosity-permeability-clay content on the velocity of compressional waves, *Geophysics*, **56**, 1930–1939.

Kowallis, B.J., Jones, L.E.A. & Wang, H.F., 1984. Velocity-porosity-clay content systematics of poorly consolidated sandstones, *Journal of Geophysical Research: Solid Earth*, **89**, 10355–10364.

Li, H., Han, D. H., Gao, J., Yuan, H. & Wang, Y., 2019. Pressure loading histories and clay fraction effects on the static and dynamic elastic properties of sand-clay synthetic sediments, *Powder Technology*, **345**, 804–814.

Li, N., Fu, L., Yang, J. & Han, T., 2021. On three-stage temperature dependence of elastic wave velocities for rocks, *Journal of Geophysics and Engineering*, **18**, 328–338.

Liu, Z., Peng, R., Li, X., Du, X., Zhu, Z., Li, X. & Li, H., 2022. Wave velocity in shale in the Wufeng-Longmaxi formation in Sichuan Basin, *Journal of Geophysics and Engineering*, **19**, 283–294.

Downloaded from https://academic.oup.com/jge/article/20/1/103/6991334 by guest on 28 June 2025

Main, I.G., Ohmyoung, K., Ngwenya, B.T. & Elphick, S.C.,2000. Fault sealing during deformation-band growth in porous sandstone, *Geology*, **28**, 1131–1134.

Marion, D., Nur, A. & Yin, H., 1992. Compressional velocity and porosity in sand-clay mixtures, *Geophysics*, **57**, 554–563.

Nie, J., Qu, Z., Cheng, Y., Wang, X., Zhu, J., Sun, S., Zhao, L & Geng, J., 2021. Diagnosing of clay distribution in argillaceous sandstone by a rock physics template, *Geophysical Prospecting*, **69** 1700–1715.

Nur, A. & Byerlee, J.D., 1971. An exact effective stress law for elastic deformation of rock with fluids, *Journal of Geophysical Research Atmospheres*, **76** 6414–6419.

Pedersen, B.K. & Nordal, K., 1999. *Petrophysical evaluation of thin beds: a review of the Thomas–Stieber approach*, *Course 24034 Report Norwegian University of Science*.

Qi, H., Ba, J. & Muller, T.M., 2021. Temperature effect on the velocity-porosity relationship in rocks. *Journal of Geophysical Research: Solid Earth*, **126**, e2019JB019317.

Thomas, E.C. & Stieber, S.J., 1975. The distribution of shale in sandstones and its effect upon porosity, *16th Annual Logging Symp, Society of Petrophysicists and Well Log Analysts*.

Thomas, E.C. & Stieber, S.J., 1977. Log derived shale distributions in sandstone and its effect upon porosity, water saturation, and permeability, *6th Formation Eval. Symp*, Canadian Well Logging Society.

Yang, S.Q. & Hu, B., 2020. Creep and permeability evolution behavior of red sandstone containing a single fissure under a confining pressure of 30Mpa, *Scientific Reports*, **10**, article no. 1900.

Zimmerman, R.W., Somerton, W.H. & King, M.S., 1986. Compressibility of porous rocks, *Journal of Geophysical Research: Solid Earth*, **91** 12765–12777.

Zuo, X., Li, C., Zhang, J., Ma, G & Chen, P., 2020. Geochemical characteristics and depositional environment of the Shahejie Formation in the Binnan Oilfield, China, *Journal of Geophysics and Engineering*, **17**, 539–551.

Downloaded from https://academic.oup.com/jge/article/20/1/103/6991334 by guest on 28 June 2025